

OPTICAL PHASE CURVES OF KEPLER EXOPLANETS

LISA J. ESTEVES

Astronomy & Astrophysics, University of Toronto, 50 St. George Street, Toronto, Ontario, Canada, M5S 3H4

ERNST J. W. DE MOOIJ

Astronomy & Astrophysics, University of Toronto, 50 St. George Street, Toronto, Ontario, Canada, M5S 3H4

RAY JAYAWARDHANA

Astronomy & Astrophysics, University of Toronto, 50 St. George Street, Toronto, Ontario, Canada, M5S 3H4

Draft version July 27, 2018

ABSTRACT

We have conducted a comprehensive search for optical phase variations of all planet candidates with tight orbits ($a/R_\star < 10$) in fifteen quarters of data from the *Kepler* space telescope. After correcting for systematics, we found eight systems that appear to show secondary eclipses as well as phase variations. Of these, five (Kepler-5, Kepler-6, Kepler-8, KOI-64 and KOI-2133) are new and three (TrES-2, HAT-P-7 and KOI-13) have previously published phase curves, albeit with many fewer observations. We model the full phase curve of each planet candidate, including the primary and secondary transits, and derive their albedos, day- and night-side temperatures, ellipsoidal variations and Doppler beaming. We find that KOI-64 and KOI-2133 have night-side temperatures well above their equilibrium values (while KOI-2133 also has an albedo > 1), so we conclude that they are likely to be self-luminous objects rather than planets. The characteristics of the six other candidates are consistent with their being planets with low geometric albedos (< 0.3). For TrES-2 and KOI-13, the *Kepler* bandpass appears to probe atmospheric layers hotter than the planet's equilibrium temperature. For KOI-13, we detect a never-before-seen third cosine harmonic with an amplitude of 6.7 ± 0.3 ppm and a phase shift of -1.1 ± 0.1 radians in the phase curve residual, which could be due to its spin-orbit misalignment. We report derived planetary parameters for all six planets, including masses from ellipsoidal variations and Doppler beaming, and compare our results to published values when available. Our results nearly double the number of *Kepler* exoplanets with measured phase curve variations, thus providing valuable new constraints on the properties of close-in hot Jupiters.

1. INTRODUCTION

Until recently, most measurements of the day-side emission of hot Jupiters have relied on targeting the secondary eclipses of these planets. Typically, these studies have focused on the thermal emission in the near- and mid-infrared using the *Spitzer* Space Telescope (e.g. review by Deming 2009) as well as ground-based telescopes (e.g. de Mooij & Snellen 2009; Croll et al. 2010). However, such observations only permit indirect measurements of the albedo and the day-night contrast of exoplanets (e.g. Cowan & Agol 2011). Phase curve measurements with *Spitzer*, on the other hand, have provided direct measurements of the day-night contrasts (e.g. Knutson et al. 2007), thus the temperature difference between the two hemispheres, and have shown that the hottest spot in the planet's atmosphere could be offset from sub-stellar point (e.g. Knutson et al. 2007).

At optical wavelengths, reflected light could account for a significant fraction of a planet's light curve. Moreover, since the planet-to-star contrast is much lower in the optical regime, contributions from ellipsoidal variations and Doppler boosting also become important.

Both these effects provide information on the planet-to-star mass ratio. Ellipsoidal variations stem from changes in the star's light due to tides raised by the planet, while Doppler boosting results from the reflex motion (K_\star) of the star. So far, optical phase curves of only a handful planets have been presented in the literature: CoRoT-1b (Snellen et al. 2009), HAT-P-7b (e.g. Borucki et al. 2009; Welsh et al. 2010), KOI-13 (e.g. Shporer et al. 2011; Mazeh et al. 2012), TrES-2b (Kipping & Spiegel 2011; Barclay et al. 2012), and Kepler 41 (Quintana et al. 2013).

The *Kepler* space telescope monitors over 150,000 stars, and so far the *Kepler* team has publicly released fifteen quarters of data, acquired over three years of continuous observations. The majority of stars only have long-cadence (LC) measurements, with a sampling rate of 29.425 minutes, while a small fraction also have short-cadence (SC) observations, with a sampling rate of 58.85 seconds (Borucki et al. 2011).

Here we present the results of our analysis of the first fifteen quarters of *Kepler* LC and SC data for eight objects (Kepler-5b, Kepler-6b, Kepler-8b, KOI-13, KOI-64, KOI-2133, TrES-2b, HAT-P-7b) that exhibit phase variations. In Section 2 we present the dataset and our analysis method, while in Section 3 we present our model to fit the data. The results are presented and discussed in Section 4, and finally we provide the

conclusions in Section 5.

2. DATA REDUCTION

After correcting for systematics (see Sec. 2.1 below), we visually inspected the phase curves of all publicly released Kepler planetary candidates and confirmed planets that have a semi-major axis to stellar radius (a/R_*) ratio of less than 10. Of these, we found 8 systems (Kepler-5, Kepler-6, Kepler-8, KOI-13, KOI-64, KOI-2133, TrES-2 and HAT-P-7) that, after the removal of systematics, exhibited an apparent phase curve signal.

2.1. Removal of Systematics

In our analysis, we used both the *Kepler* LC and SC simple aperture photometry (SAP) data available (see Table 1). Instrumental signals were removed by performing a linear least squares fit¹ of the first eight cotrending basis vectors (CBVs) (Fanelli et al. 2011) to the time-series of each quarter individually. Before cotrending, we removed any bad data points flagged by *Kepler* in the SAP or CBV files and to prevent contamination we only fit the CBVs to the out-of-transit time-series. The fitted basis vectors were then divided out of the quarter, in order to preserve the amplitude of the physical signals of interest. Since CBVs are only provided for the LC data, we interpolated onto the SC time-stamps using cubic splines.

In order to remove quarter-to-quarter discontinuities

TABLE 1
Kepler QUARTERS OF DATA USED IN ANALYSIS

System	SC Quarter	LC Quarters
Kepler-5	2, 3, 4, 5, 6, 7, 8, 9 10, 11, 12	0, 1, 13, 14 —
Kepler-6	2, 3, 4, 5, 6, 9, 10 11, 12, 13	0, 1, 8, 14
Kepler-8	2, 3, 4, 5, 6, 7, 9, 10 11, 12, 13	0, 1, 8, 14
KOI-64	3, 4, 5, 6, 7, 8, 9, 10 11, 12, 13	0, 1, 2, 14
KOI-2133	—	0, 1, 2, 3, 4, 5, 6, 7, 8 9, 10, 11, 12, 13, 14
TrES-2	0, 1, 2, 3, 5, 6, 7, 9 10, 11, 13, 14	—
HAT-P-7	0, 1, 2, 3, 4, 5, 6, 7 8, 9, 10, 11, 12, 13, 14	—
KOI-13	2, 3, 7, 8, 9, 10, 11 12, 13, 14	0, 1, 4, 5, 6

we normalized each quarter to its out-of-transit median. After cotrending and combining all quarters we removed outliers by calculating a running median and standard deviation of 21 measurements around each point and rejecting measurements that differed by more than 3σ . We also calculated the out-of-transit median for each half of the planet’s orbit, where an orbit is defined as the time between two consecutive transits, and removed any orbits whose median deviated by more than 2σ . This was done to remove sections of the light

curve where the CBV fit poorly without introducing a phase curve sampling bias. The raw, cotrended and cotrended/out-of-transit/outlier-filtered light curve, of each system, can be found in Figs. 1-4.

2.2. Companion Stars

Kepler’s large pixel size, with a width of $3.98''$, allows for the possibility of dilution from a background or foreground star or a nearby stellar companion. In the literature, we find that several of our 8 systems have 1 or 2 companion stars within $4''$ of the planetary host star (see Table 2). However, the only system that is significantly diluted by its companion is KOI-13, which we have corrected for as the contamination would greatly affect the derived planetary parameters. Note that each of these systems could also have closer companions that could not be detected by previous studies and that they could significantly dilute our results.

TABLE 2
DETECTED STELLAR COMPANIONS AROUND PLANET HOST STARS

Host Star	Host Star Kp Mag	Comp. Dist (")	Comp. Est. Kep Mag	Comp. Est. Flux %
Kepler-5	13.369 ^b	0.9 ^b	18.7	<1%
		3.39 ^b	19.8	<1%
Kepler-6	13.303 ^b	— ^b	—	—
Kepler-8	13.563 ^b	3.04 ^b	22.1	<1%
		3.74 ^b	20.5	<1%
KOI-64	13.143 ^b	— ^b	—	—
KOI-2133	12.495 ^c	— ^a	—	—
TrES-2	11.338 ^c	0.9 ^d	—	<1%
HAT-P-7	10.463 ^c	— ^e	—	—
KOI-13	9.958 ^b	1.12 ^b	10.5	38%

^a No data is available.

^b From Adams et al. (2012).

^c From Batalha et al. (2013).

^d From Daemgen et al. (2009).

^e From Narita et al. (2010).

2.3. Stellar Variability

The periodogram (Zechmeister & Kürster 2009) of KOI-64 revealed a strong periodic signal, sharply peaked at a period of 2.224 days, with variations in phase and amplitude between oscillations. We modeled the variability of 2.224-day segments using a linear polynomial and a sine wave with a 2.224-day period, while allowing for small shifts in phase between segments. To minimize discontinuities between periods we simultaneously fit half a period on either side of each segment, then stitched the segments together by interpolating cubic splines over the first and last 10%. The light curve before and after variability removal can be found in the *lower* plot of Fig. 2.

Periodograms of the other systems showed that, close to the planet’s period or aliases of the period, the stellar variability had an amplitude much lower than the phase curve signal.

¹ Using custom IDL procedures.

We modeled the transit and phase curve separately and in two stages in order to remove the phase curve baseline from the transit light curve.

3.1. Transit Modeling

To model the transit we used a Mandel & Agol (2002) transit model for a quadratically limb darkened source, over an orbital phase of -0.1 to 0.1, which we fit to our data using a Markov Chain Monte Carlo simulation. The simulation simultaneously fit for the impact parameter of the transit (b), the semi-major axis of the planet's orbit to star radius (a/R_*), the planet to star radius (r/R_*) and the linear and quadratic limb-darkening coefficients (γ_1 and γ_2). Five sequences of 100,000 steps were generated and the first 30,000 points were trimmed to avoid any contamination from the initial conditions. The chains were then combined after checking that they were well mixed (Gelman & Rubin 1992).

The transit curve of KOI-13 is asymmetric as a result of the planet's motion across a stellar surface temperature gradient during transit (Szabó et al. 2011). To obtain a symmetric curve we averaged the transit in 30-second bins, reflected the curve onto itself and took the mean of each bin. Fitting this curve provided a good first order approximation of the transit depth and shape.

3.2. Phase Curve Modeling

We modeled the normalized, out-of-transit phase curve as a sum of four contributions: i) F_p , the planet's phase function; ii) F_{ecl} , the secondary eclipse, when the light from the planet is blocked as it passes behind its host star; iii) F_d , the Doppler boost caused by the host star's changing radial velocity; iv) F_e , the ellipsoidal variations resulting from tides on the star raised by the planet. Each of these components is phase (ϕ) dependent with ϕ running from 0 to 1 and mid-transit occurring at $\phi=0$. The change in brightness of the planet-star system as a function of phase can then be described by

$$\frac{\Delta F}{F} = f_0 + F_{\text{ecl}}(\phi) + F_p(\phi) + F_d(\phi) + F_e(\phi) \quad (1)$$

where f_0 is an arbitrary zero-point in flux. The details of phase curve model fit are the same as described in Sec. 3.1.

3.3. Secondary Eclipse

Since each of these systems appear to have a secondary eclipse centered on $\phi=0.5$, we assume that the orbits have zero eccentricity and model the secondary eclipse using the formalism from Mandel & Agol (2002) for a uniform source.

3.4. Phase Function

We model the variation in planetary light as a Lambert sphere (Russell 1916) described by

$$F_p = A_p \frac{\sin z + (\pi - z) \cos z}{\pi} \quad (2)$$

where A_p is the amplitude of the phase function and z is related to ϕ and the orbital inclination (i) through

$$\cos(z) = -\sin(i) \cos(2\pi\phi) \quad (3)$$

3.5. Doppler Boosting

Doppler boosting is a combination of a bolometric and a bandpass dependent effect. The bolometric effect is the result of non-relativistic Doppler boosting of the stellar light in the direction of the star's radial velocity. The observed periodic brightness change is proportional to the star's radial velocity, which is a function of the planet's distance and mass (Barclay et al. 2012). The bandpass dependent effect is a periodic red/blue shift of the star's spectrum, which results in a periodic measured brightness change as parts of the star's spectrum move in and out of the observed bandpass (Barclay et al. 2012). The amplitude of the Doppler boosting is modeled by

$$F_d = A_d \sin(2\pi\phi) \quad (4)$$

where A_d is the amplitude of the Doppler boost. Given that the radial velocities are much lower than the speed of light and that the planet has zero eccentricity, A_d can be parameterized by

$$A_d = \alpha_d \frac{K_*}{c} \quad (5)$$

Here, c is the speed of light, α_d is the photon-weighted bandpass-integrated beaming factor and K_* is the radial velocity semi-amplitude given by

$$K_* = \left(\frac{2\pi G}{P} \right)^{1/3} \frac{M_p \sin i}{M_*^{2/3}} \quad (6)$$

where G is the universal gravitational constant, P is the orbital period of the planet and we have assumed $M_p \ll M_*$. Similar to Barclay et al. (2012), we calculated α_d in the manner described by Bloemen et al. (2011) and Loeb & Gaudi (2003).

$$\alpha_b = \frac{\int T_K \left(5 + \frac{d \ln F_{\lambda,*}}{d \ln \lambda} \right) \lambda F_{\lambda,*} d\lambda}{\int T_K \lambda F_{\lambda,*} d\lambda} \quad (7)$$

T_K is the Kepler transmission function, λ is the wavelength and $F_{\lambda,*}$ is the stellar flux computed using the NEXTGEN model spectra (Hauschildt et al. 1999).

We opted to fit Kepler-5, Kepler-6, and KOI-2133 without Doppler boosting as they exhibit a poorly constrained, negative Doppler signal.

3.6. Ellipsoidal Variations

Ellipsoidal variations are periodic changes in observed stellar flux caused by fluctuations of the star's visible surface area as the stellar tide, created by the planet, rotates in and out of view of the observer (Mislis et al. 2012). If there is no tidal lag, the star's visible surface area and ellipsoidal variations are at maximum when the direction of the tidal bulge is perpendicular to the observer's line of sight and at minimum during the transit and secondary eclipse.

The ellipsoidal light curve is described, by Eqs. 1-3 of Morris (1985), as a linear combination of the first three cosine harmonics of the planet's period. These equations can be re-expressed as

$$F_e = -A_e [\cos(2\pi \cdot 2\phi) + f_1 \cos(2\pi\phi) + f_2 \cos(2\pi \cdot 3\phi)] \quad (8)$$

TABLE 3
LIMB DARKENING, GRAVITY DARKENING AND HIGHER-ORDER ELLIPSOIDAL COEFFICIENTS

	Kepler-5	Kepler-6	Kepler-8	KOI-64	KOI-2133	TrES-2	HAT-P-7	KOI-13
u	0.290	0.398	0.298	0.474	0.549	0.354	0.282	0.624
y	0.545	0.628	0.549	0.650	0.733	0.580	0.551	0.476
f_1	0.0154	0.0173	0.0139	0.0288	0.0403	0.0142	0.0214	0.0460
f_2	0.0259	0.0288	0.0242	0.0622	0.0672	0.0247	0.0378	0.0779

A_e is the amplitude of the dominant cosine harmonic and f_1 and f_2 are fractional constants defined by

$$f_1 = 3\alpha_1 \left(\frac{a}{R_\star}\right)^{-1} \frac{5 \sin^2 i - 4}{\sin i} \quad (9)$$

$$f_2 = 5\alpha_1 \left(\frac{a}{R_\star}\right)^{-1} \sin i \quad (10)$$

A_e is parameterized as

$$A_e = \alpha_2 \frac{M_p}{M_\star} \left(\frac{a}{R_\star}\right)^{-3} \sin^2 i \quad (11)$$

where M_\star is the mass of the star and M_p is the mass of the planet; the only free parameter in our fit of the ellipsoidal variations. The constants α_1 and α_2 are defined as

$$\alpha_1 = \frac{25u}{24(15+u)} \left(\frac{y+2}{y+1}\right) \quad (12)$$

$$\alpha_2 = \frac{3(15+u)}{20(3-u)}(y+1) \quad (13)$$

where u and y are the linear limb darkening and gravity darkening parameters, respectively. Similar to Barclay et al. (2012) we trilinearly interpolate for u and y calculated by Claret & Bloemen (2011) from the grids in effective temperature, surface gravity and metallicity using the *Kepler* filter, a microturbulent velocity of 2 km s^{-1} and ATLAS model spectra (See Table 3).

4. RESULTS AND DISCUSSION

The relevant stellar, fitted and derived parameters can be found in Tables 4-5 and plots of the transit and phase curve fit and residuals, for each system, can be found in Figs. 1-3.

4.1. Derived Masses

We compared the Kepler-5, Kepler-6, Kepler-8, TrES-2 and HAT-P-7 mass values from radial velocity measurements to the planet masses derived from ellipsoidal variations (see Tables 4-5). We find that TrES-2 (O'Donovan et al. 2006) and HAT-P-7 (Pál et al. 2008) agree with our ellipsoidal mass, while Kepler-6 (Dunham et al. 2010) and Kepler-8 (Jenkins et al. 2010) are 2σ lower and Kepler-5 (Koch et al. 2010) is 3σ higher than our value.

Of these planets, we also derived planet masses from the Doppler boosting signal for Kepler-8, TrES-2 and HAT-P-7 (see Tables 4-5). We find that Kepler-8's Doppler mass is consistent with zero while HAT-P-7's is over 9σ higher than its mass from ellipsoidal and radial velocity measurements. TrES-2's is in agreement with both.

We also compare our ellipsoidal and Doppler measurements with the previously published phase curves of TrES-2, HAT-P-7 and KOI-13.

For TrES-2, our ellipsoidal and Doppler amplitudes agree within 1σ to values in Barclay et al. (2012) and 2σ to values in Kipping & Spiegel (2011).

For HAT-P-7, Jackson et al. (2012) gives a planet to stellar mass ratio of $(1.10 \pm 0.06) \cdot 10^{-3}$ and a radial velocity semi-amplitude of $300 \pm 70 \text{ m s}^{-1}$. Using our formalism this corresponds to $A_e = 20 \pm 1 \text{ ppm}$ and $A_d = 3.4 \pm 0.8$, which are within 1σ and 3σ of our values, respectively. In addition, Mislis et al. (2012) find an ellipsoidal and Doppler amplitude of 31 ppm and 8.7 ppm, respectively, while Welsh et al. (2010) measure $A_e = 37.3$. These values are approximately double ours, however this is because Mislis et al. (2012) and Welsh et al. (2010) measure peak-to-peak amplitudes, while we measure semi-amplitudes. Another study, Van Eylen et al. (2012), measured an ellipsoidal amplitude of 59 ± 1 , however their model, compared to ours, includes an additional factor of π . If we take this into account we find that our values agree.

For KOI-13, Mazeh et al. (2012) and Shporer et al. (2011) find ellipsoidal values of 66.8 ± 1.6 and $30.25 \pm 0.63 \text{ ppm}$, respectively, and Doppler values of 8.6 ± 1.1 and $5.28 \pm 0.44 \text{ ppm}$, respectively. Note that Shporer et al. (2011) do not correct for the dilution from KOI-13's companion star and as a result calculate much lower values. From their phase curve analysis, Mislis & Hodgkin (2012) give a planet mass of $8.3 \pm 1.25 M_J$, which is in agreement with our derived mass.

Each of these studies use a different number of observations, systematic removal method and phase curve model. In particular the choice of phase function will influence the derived ellipsoidal mass. As described in Mislis et al. (2012), there is a degeneracy between the choice of phase function and amplitude of the ellipsoidal variations. Choosing a wider phase function, such as a geometrical sphere, will result in a lower ellipsoidal amplitude.

4.2. 3ϕ Signal

It is very clear that there is a 3ϕ signal present in the phase curve residual of KOI-13 (see Fig. 3, *middle* panel). We have re-modeled KOI-13's phase curve to include the 3ϕ cosine signal (see Fig. 3, *lower* panel) and found a significant amplitude ($A_{3\phi} = 6.7 \pm 0.3 \text{ ppm}$) and phase shift ($\theta_{3\phi} = -1.1 \pm 0.1 \text{ radians}$). Note that this also slightly changed the fitted phase curve parameters (see Table 5).

The host star of KOI-13 is a rapid rotator ($v \sin i = 65 \text{ km s}^{-1}$), and therefore has significant gravity darkening at the equator compared to the star's poles. This is clearly seen in the asymmetry

TABLE 4
STELLAR AND PLANETARY PARAMETERS

Parameter	Kepler-5	Kepler-6	Kepler-8	KOI-64
Period (Days) ^a	3.5484657 ± 0.0000007	3.2346995 ± 0.0000004	3.522297 ± 0.0000007	1.9510914 ± 0.000004
T_0 (BJD-2454900) ^a	55.90078 ± 0.00007	54.48580 ± 0.00004	54.11860 ± 0.00062	90.54077 ± 0.00052
T_* (K)	6297 ± 60 ^b	5647 ± 44 ^c	6213 ± 150 ^d	5128 ± 200 ^a
log g (cgs)	3.96 ± 0.10 ^b	4.236 ± 0.011 ^c	4.28 ± 0.10 ^d	3.94 ± 0.5 ^a
[Fe/H]	0.04 ± 0.06 ^b	0.34 ± 0.04 ^c	-0.055 ± 0.03 ^d	-0.341 ± 0.5 ^a
R_*/R_\odot	1.793 ^{+0.043} _{-0.062} ^b	1.391 ^{+0.017} _{-0.034} ^c	1.486 ^{+0.053} _{-0.062} ^d	1.938 ^a
M_*/M_\odot	1.374 ^{+0.008} _{-0.059} ^b	1.209 ^{+0.044} _{-0.038} ^c	1.213 ^{+0.062} _{-0.063} ^d	1.19 ^a
Transit Fit				
R_p/R_*	0.078845 ^{+0.000047} _{-0.000056}	0.092853 ^{+0.000037} _{-0.000045}	0.094337 ^{+0.000099} _{-0.000085}	0.04038 ^{+0.00040} _{-0.00051}
a/R_*	6.365 ^{+0.019} _{-0.014}	7.5606 ^{+0.0034} _{-0.0031}	6.820 ^{+0.017} _{-0.018}	3.972 ^{+0.070} _{-0.078}
b	0.188 ^{+0.011} _{-0.017}	0.032 ^{+0.011} _{-0.013}	0.7212 ± 0.0021	0.9324 ^{+0.0049} _{-0.0039}
i (degrees)	88.31 ^{+0.16} _{-0.10}	89.759 ^{+0.099} _{-0.082}	83.929 ^{+0.033} _{-0.034}	76.42 ^{+0.29} _{-0.35}
γ_1	0.3494 ^{+0.0039} _{-0.0032}	0.4691 ^{+0.0034} _{-0.0073}	0.305 ^{+0.023} _{-0.014}	0.466 ^{+0.045} _{-0.035}
γ_2	0.1711 ^{+0.0044} _{-0.0052}	0.1762 ^{+0.0173} _{-0.0059}	0.252 ^{+0.012} _{-0.032}	0.306 ^{+0.041} _{-0.039}
Phasecurve Fit				
F_{ecl} (ppm)	18.8 ± 3.7	8.9 ± 3.8	26.2 ± 5.6	61.4 ± 3.8
F_n (ppm)	2 ± 4	-4 ± 4	0.8 ± 6	49 ± 4
A_p (ppm)	16.5 ± 2.0	12.4 ± 2.0	25.3 ^{+2.7} _{-2.6}	12.5 ^{+1.8} _{-1.9}
A_d (ppm)	—	—	2.5 ± 1.2	3.05 ± 0.80
A_e (ppm)	4.7 ^{+1.0} _{-1.1}	2.7 ± 1.0	4.0 ± 1.4	15.20 ± 0.93
Derived Parameters				
R_p (R_J)	1.406 ^{+0.034} _{-0.049}	1.285 ^{+0.016} _{-0.031}	1.395 ^{+0.050} _{-0.058}	0.779 ± 0.041
a (Au)	0.0531 ^{+0.0013} _{-0.0018}	0.04889 ^{+0.00060} _{-0.00120}	0.0471 ^{+0.0017} _{-0.0020}	0.0358 ^{+0.0019} _{-0.0020}
M_p from A_d (M_J)	—	—	1.85 ^{+0.90} _{-0.88}	1.52 ± 0.41
M_p from A_e (M_J)	1.34 ^{+0.30} _{-0.31}	1.02 ± 0.40	1.23 ± 0.43	0.829 ^{+0.097} _{-0.099}
Weighted M_p (M_J)	—	—	1.35 ± 0.39	0.867 ± 0.095
$A_{g,\text{ecl}}$	0.122 ± 0.024	0.059 ± 0.025	0.137 ± 0.029	0.594 ^{+0.042} _{-0.044}
$T_{\text{eq,max}}$ (K)	2260	1860	2150	2320
$T_{\text{eq,hom}}$ (K)	1760	1450	1680	1820
$T_{\text{B,day}}$ (K)	2400 ⁺⁵⁰ ₋₆₀	2000 ⁺⁸⁰ ₋₁₀₀	2370 ⁺⁵⁰ ₋₇₀	2940 ⁺²⁰ ₋₃₀
$T_{\text{B,night}}$ (K)	<2100(1 σ) <2300(3 σ)	<1600(1 σ) <2000(3 σ)	<2100(1 σ) <2300(3 σ)	2850 ± 30

^a From Batalha et al. (2013).

^b From Koch et al. (2010).

^c From Dunham et al. (2010).

^d From Jenkins et al. (2010).

Note: A stellar mass uncertainty of $\pm 0.1M_\odot$ and a stellar radius uncertainty of $\pm 0.1R_\odot$ was assumed when not given in the literature.

in the transit caused by a spin-orbit misalignment (Szabó et al. 2011; Barnes et al. 2011). This signal, at three times the orbital frequency, could be due to the tidal bulge caused by the planet, moving across areas with different surface brightnesses.

4.3. Secondary Eclipse and Planetary Phase-function

For all the systems we detect a significant secondary eclipse and phase function and for KOI-13, KOI-64, KOI-2133 and HAT-P-7 we also detect a significant night-side flux (F_n) defined as

$$F_n = F_{\text{ecl}} - A_p \quad (14)$$

where F_{ecl} is the depth of the eclipse and A_p is the amplitude of the phase function (see Tables 4-5).

All systems, except KOI-2133 and Kepler-8, have a published secondary eclipse detection of greater than 1σ . Of these, KOI-13, TrES-2 and HAT-P-7 also have published phase functions and therefore night-side flux measurements.

For TrES-2, our measurements agree with the secondary eclipse and phase function values presented in Barclay et al. (2012) and Kipping & Spiegel (2011).

For HAT-P-7, the secondary eclipse and phase function values in the literature differ significantly from each other. Our values agree with Morris et al. (2013) and Coughlin & López-Morales (2012) and are within 4σ of the values presented in Jackson et al. (2012), and Van Eylen et al. (2012). In addition, Borucki et al. (2009), who analyze 10 days of data, measure $F_{\text{ecl}} = 130 \pm 11$ ppm and $A_p = 122$ ppm, while Welsh et al. (2010) use 34 days of data and find $F_{\text{ecl}} = 85.8$ ppm and $A_p = 63.7$ ppm. The large discrepancy between these two studies and our analysis, which includes over 1000 days of data, is most likely due to the number of observations used.

For KOI-13, the secondary eclipse values from Szabó et al. (2011) and Coughlin & López-Morales (2012) are within 2σ of our value. While Mazeh et al. (2012) measure $F_{\text{ecl}} = 163.8 \pm 3.8$ ppm, 4σ higher than our value, and a phase function semi-amplitude of 72 ± 1.5

TABLE 5
STELLAR AND PLANETARY PARAMETERS

Parameter	KOI-2133	TrES-2	HAT-P-7	KOI-13	
Period (Days) ^a	6.2465796 ± 0.000082	2.4706132 ± 0.0000001	2.2047355 ± 0.0000001	1.7635877 ± 0.000001	
T_0 (BJD-2454900) ^a	69.39661 ± 0.0048	55.76257 ± 0.00001	54.35780 ± 0.00002	53.56513 ± 0.00001	
T_* (K)	4712 ± 200 ^a	5850 ± 50 ^e	6350 ± 80 ^f	8511 ± 1 ^g	
$\log g$ (cgs)	2.852 ± 0.5 ^a	4.4 ± 0.1 ^e	4.07 ^{+0.04} _{-0.08} ^f	3.9 ± 0.1 ^g	
[Fe/H]	0.509 ± 0.5 ^a	-0.15 ± 0.10 ^e	0.26 ± 0.08 ^f	0.2 ^g	
R_*/R_\odot	7.488 ^a	1.000 ^{+0.036} _{-0.033} ^e	1.84 ^{+0.23} _{-0.11} ^f	2.55 ^g	
M_*/M_\odot	2.25 ^a	0.980 ± 0.062 ^e	1.47 ^{+0.08} _{-0.05} ^f	2.05 ^g	
Transit Fit					
R_p/R_*	0.01775 ^{+0.00042} _{-0.00065}	0.125106 ^{+0.000025} _{-0.000024}	0.077490 ± 0.000013	0.080509 ^{+0.000033} _{-0.000048}	
a/R_*	4.51 ^{+0.12} _{-0.26}	7.8957 ^{+0.0028} _{-0.0027}	4.1512 ^{+0.0025} _{-0.0026}	4.3396 ^{+0.0102} _{-0.0075}	
b	0.0 ^{+0.19} _{-0.26}	0.84388 ^{+0.00020} _{-0.00026}	0.4973 ^{+0.0011} _{-0.0010}	0.3681 ^{+0.0041} _{-0.0064}	
i (degrees)	89.9 ^{+3.3} _{-2.5}	83.8646 ^{+0.0041} _{-0.0036}	83.119 ± 0.019	85.135 ^{+0.097} _{-0.063}	
γ_1	0.69 ± 0.12	0.3529 ^{+0.0024} _{-0.0021}	0.3522 ^{+0.0012} _{-0.0010}	0.3047 ^{+0.0033} _{-0.0038}	
γ_2	0.05 ^{+0.25} _{-0.12}	0.2635 ^{+0.0031} _{-0.0030}	0.1705 ^{+0.0010} _{-0.0019}	0.2249 ^{+0.0072} _{-0.0063}	
Phasecurve Fit					
F_{ecl} (ppm)	38.7 ± 8.2	7.5 ± 1.7	68.31 ± 0.69	147.24 ± 0.82	143.0 ^{+1.2} _{-1.4}
F_{n} (ppm)	30 ± 10	3 ± 2	2.6 ± 0.8	19 ± 1	17 ⁺¹ ₋₂
A_p (ppm)	13.1 ^{+5.8} _{-6.0}	4.77 ^{+0.65} _{-0.63}	65.75 ± 0.48	128.67 ^{+0.59} _{-0.58}	125.96 ^{+0.82} _{-0.91}
A_d (ppm)	—	2.40 ± 0.30	5.80 ± 0.19	7.14 ± 0.24	7.23 ^{+0.25} _{-0.24}
A_e (ppm)	45.2 ± 3.1	3.67 ± 0.33	19.09 ± 0.25	61.28 ± 0.31	60.97 ± 0.32
$A_{3\phi}$ (ppm)	—	—	—	—	6.71 ± 0.26
$\theta_{3\phi}$ (rad)	—	—	—	—	-1.119 ^{+0.096} _{-0.148}
Derived Parameters					
R_p (R_J)	1.322 ^{+0.036} _{-0.051}	1.245 ^{+0.045} _{-0.041}	1.418 ^{+0.177} _{-0.085}	2.042 ± 0.080	
a (Au)	0.1569 ^{+0.0047} _{-0.0091}	0.0367 ^{+0.0013} _{-0.0012}	0.0355 ^{+0.0044} _{-0.0021}	0.0514 ± 0.0020	
M_p from A_d (M_J)	—	1.28 ± 0.17	4.25 ^{+0.21} _{-0.17}	8.49 ± 0.40	8.61 ^{+0.41} _{-0.40}
M_p from A_e (M_J)	5.92 ^{+0.68} _{-1.12}	1.37 ± 0.15	1.631 ^{+0.091} _{-0.060}	7.45 ± 0.37	7.41 ± 0.37
Weighted M_p (M_J)	—	1.33 ± 0.11	1.985 ± 0.070	7.93 ± 0.27	7.95 ± 0.27
$A_{\text{g,ecl}}$	2.49 ^{+0.55} _{-0.60}	0.0301 ± 0.0069	0.1960 ± 0.0020	0.4278 ^{+0.0031} _{-0.0028}	0.4153 ^{+0.0040} _{-0.0043}
$T_{\text{eq,max}}$ (K)	2009	1880	2820	3690	3690
$T_{\text{eq,hom}}$ (K)	1570	1470	2200	2890	2890
$T_{\text{B,day}}$ (K)	3300 ± 100	1910 ⁺⁴⁰ ₋₅₀	2846 ± 4	3724 ± 3	3706 ⁺⁵ ₋₆
$T_{\text{B,night}}$ (K)	3100 ± 200	1700 ⁺⁸⁰ ₋₂₀₀	1950 ⁺⁶⁰ ₋₇₀	2740 ± 20	2710 ⁺³⁰ ₋₄₀

^a From Batalha et al. (2013).

^e From Szabó et al. (2011).

^f From Sozzetti et al. (2007).

^g From Pál et al. (2008).

Note: A stellar mass uncertainty of $\pm 0.1M_\odot$ and a stellar radius uncertainty of $\pm 0.1R_\odot$ was assumed when not given in the literature and for KOI-13, the *right* column contains results from a model fit including the 3ϕ term, while the *left* column is without.

ppm, which, if converted to a peak-to-peak amplitude, is a 8σ higher than ours. In addition, Shporer et al. (2011) measure a phase function semi-amplitude of 39.78 ± 0.52 , approximately half our semi-amplitude, due to not removing the dilution from KOI-13's companion.

The published eclipse depths of Kepler-5 (Désert et al. 2011) and KOI-64 (Coughlin & López-Morales 2012) agree with our values while Désert et al. (2011), who also examined Kepler-6, using Q0-5 of *Kepler* pre-search data conditioned (PDC) data, found an eclipse depth of 22 ± 7 , more than double ours. However, our analysis of Kepler-6 includes an additional eight quarters of data and uses cotrended SAP data, which exhibits fewer residual systematics when compared to PDC data (Still & Barclay 2012).

4.4. Planetary Temperatures and Albedos

If the phase function is composed solely of reflected light the planet's albedo can be described by

$$F_{\text{ecl}} = A_g \left(\frac{R_p}{a} \right)^2 \quad (15)$$

where A_g is the geometric albedo. Based on the eclipse depth and assuming that there is no contribution from thermal emission, we calculate an albedo of less than 1 for all planets, except KOI-2133 (see Tables 4-5). We consider this strong evidence for KOI-2133 being a self-luminous object and most likely not a planet. We note that the albedo calculated in this way should be considered as an upper-limit, since for all these objects thermal emission can contribute significantly (see below).

Previous observations of hot Jupiters indicate low albedos at optical wavelengths (e.g. Collier Cameron et al. 2002; Leigh et al. 2003; Rowe et al. 2006;

TABLE 6
SELF-CONSISTENT ALBEDOS AND TEMPERATURES

Parameter	Kepler-5	Kepler-6	Kepler-8	KOI-64	TrES-2	HAT-P-7	KOI-13
$A_{g,\max}$	0.065 ± 0.031	0.038 ± 0.028	0.098 ± 0.035	0.59337 ± 0.037	$0.0041^{+0.0076}_{-0.0077}$	0.0299 ± 0.0039	$0.092^{+0.027}_{-0.036}$
$A_{g,\text{hom}}$	0.119 ± 0.025	0.058 ± 0.025	0.134 ± 0.030	0.59358 ± 0.037	$0.0287^{+0.0069}_{-0.0070}$	0.1849 ± 0.0021	$0.4031^{+0.0039}_{-0.0046}$
Max A_g	—	—	—	—	0	$0.261^{+0.059}_{-0.049}$	$0.148^{+0.027}_{-0.023}$
Derived Temperatures							
$T_{B,\max}$ (K)	2198^{+28}_{-29}	1829 ± 20	2066^{+31}_{-32}	1340^{+150}_{-220}	1878.3 ± 5.4	$2784.1^{+4.3}_{-4.2}$	3558^{+54}_{-42}
$T_{B,\text{hom}}$ (K)	1681 ± 19	1420 ± 15	1590^{+22}_{-23}	1050^{+110}_{-170}	1456.0 ± 4.0	2032.0 ± 2.2	$2290.9^{+9.9}_{-8.6}$

Note: For KOI-13, the results are from a model fit including a 3ϕ term.

for an ensemble of planets), consistent with theoretical models (Burrows et al. 2008).

The albedo plays a direct role in the planet’s equilibrium temperature, T_{eq} , which can be calculated using the method of López-Morales & Seager (2007) as

$$T_{\text{eq}} = T_{\star} \left(\frac{a}{R_{\star}} \right)^2 [f(1 - A_{\text{B}})]^{1/4} \quad (16)$$

where A_{B} is the Bond albedo, which, if we assume Lambert’s law, we can be defined as $A_{\text{B}} = \frac{3}{2}A_{\text{g}}$. The re-radiation factor, f , has two extremes, $f=1/4$, corresponding to homogeneous re-distribution of energy across the planet, and, $f=2/3$, for instant re-radiation from the day-side, resulting in a very hot day-side and cold night-side. Although these two limiting cases are useful when calculating the equilibrium temperature, the true f lies somewhere in between. The equilibrium temperature can be compared to the brightness temperature T_{B} , the temperature of a black-body with the equivalent flux in the band-pass, which can be calculated as

$$F_{\text{ecl}} = \left(\frac{R_{\text{p}}}{R_{\star}} \right)^2 \frac{\int B_{\lambda}(T_{\text{B}})T_{\text{K}}d\lambda}{\int (T_{\text{K}}F_{\lambda,\star}d\lambda)} \quad (17)$$

where B_{λ} is the Planck function as a function of T_{B} and T_{K} and $F_{\lambda,\star}$ are as described in Sec. 3.5. This provides us with the brightness temperature of the planet’s day-side. In addition, if we change F_{ecl} with F_{n} , the flux from the planet’s night-side, we can calculate the night-side brightness temperature $T_{\text{B,night}}$.

In the case of isothermal atmospheric emission, we would expect that T_{B} fall somewhere between $T_{\text{eq,hom}}$ and $T_{\text{eq,max}}$ and that $T_{\text{B,night}}$ be less than $T_{\text{eq,hom}}$. However, we find that for all planets, except TrES-2, the brightness temperature is actually greater than maximum equilibrium temperature and that, for TrES-2, KOI-64 and KOI-2133, the night-side temperature is greater than the homogeneous equilibrium temperature (see Tables 4-5).

For KOI-2133, this, along with having an albedo >1 , implies that is almost certainly a self-luminous object. For KOI-64, the very large discrepancy between the night-side and equilibrium temperature also suggests that it is most-likely self-luminous and not a planet. For TrES-2, the 1.2σ difference is not significant, and can easily arise if the layers probed at optical wavelengths are at a higher temperature than the equilibrium temperature.

Since KOI-13 and HAT-P-7 have a significant night-side flux detection, consistent with their homogeneous temperature, we can place a constraint on their maxi-

mum allowed albedo. This is calculated by assuming a uniform temperature across the planet’s surface ($f=1/4$) equal to the night-side temperature derived from F_{n} . For KOI-13 and HAT-P-7, we find a maximum albedo of 0.26 and 0.148, respectively.

In general, the eclipse depths at optical wavelengths are likely a combination of reflected light and thermal emission. To investigate this we self-consistently solve for the eclipse depth as a function of A_{g} using

$$F_{\text{ecl}} = \left(\frac{R_{\text{p}}}{R_{\star}} \right)^2 \frac{\int B_{\lambda}(T_{\text{B,day}})T_{\text{K}}d\lambda}{\int (T_{\text{K}}F_{\lambda,\star}d\lambda)} + A_{\text{g}} \left(\frac{R_{\text{p}}}{a} \right)^2 \quad (18)$$

where we assume that $T_{\text{B,day}}=T_{\text{eq}}(A_{\text{B}} = \frac{3}{2}A_{\text{g}})$ as given in Eq.16. In the limit of $f=1/4$ (uniform temperature) this will provide an upper limit on A_{g} and a lower limit on $T_{\text{B,day}}$. While if $f=2/3$, we will obtain the opposite. We find that for all planets, except KOI-2133, there is a physical solution that satisfies these equations (see Table 4.4) and that all, except KOI-64, have albedos less than 0.3.

For KOI-13, if we assume a homogeneous heat distribution, an albedo of, at most, 0.148 is needed to produce the observed night-side flux. Using this albedo limit, we calculate an expected day-side flux significantly lower than the observed day-side flux. However, this would not be a problem in the case where the emitting layers probed in the *Kepler* bandpass, are hotter than the equilibrium temperature, as inferred for CoRoT-2 (Snellen et al. 2010). For TrES-2, this is most-likely also the case.

5. CONCLUSIONS

We have presented new phase curves for five *Kepler* objects of interest (Kepler-5, Kepler-6, Kepler-8, KOI-64 and KOI-2133) and re-examined the phase curves of TrES-2, HAT-P-7 and KOI-13 using 15 quarters of *Kepler* data.

The fitted and derived parameters, for each of these systems, can be found in Tables 4-5. The derived ellipsoidal masses of Kepler-5, Kepler-6, Kepler-8, TrES-2 and HAT-P-7 are within 3σ , of their published radial velocity measurements, while the derived Doppler mass for TrES-2 and HAT-P-7 is within 1σ and 9σ , respectively. When we compared the ellipsoidal and Doppler amplitudes of HAT-P-7 and KOI-13 to five previous studies that listed uncertainty values, we found that our results were within 3σ , while our values for TrES-2 agreed with its two previous phase curve studies

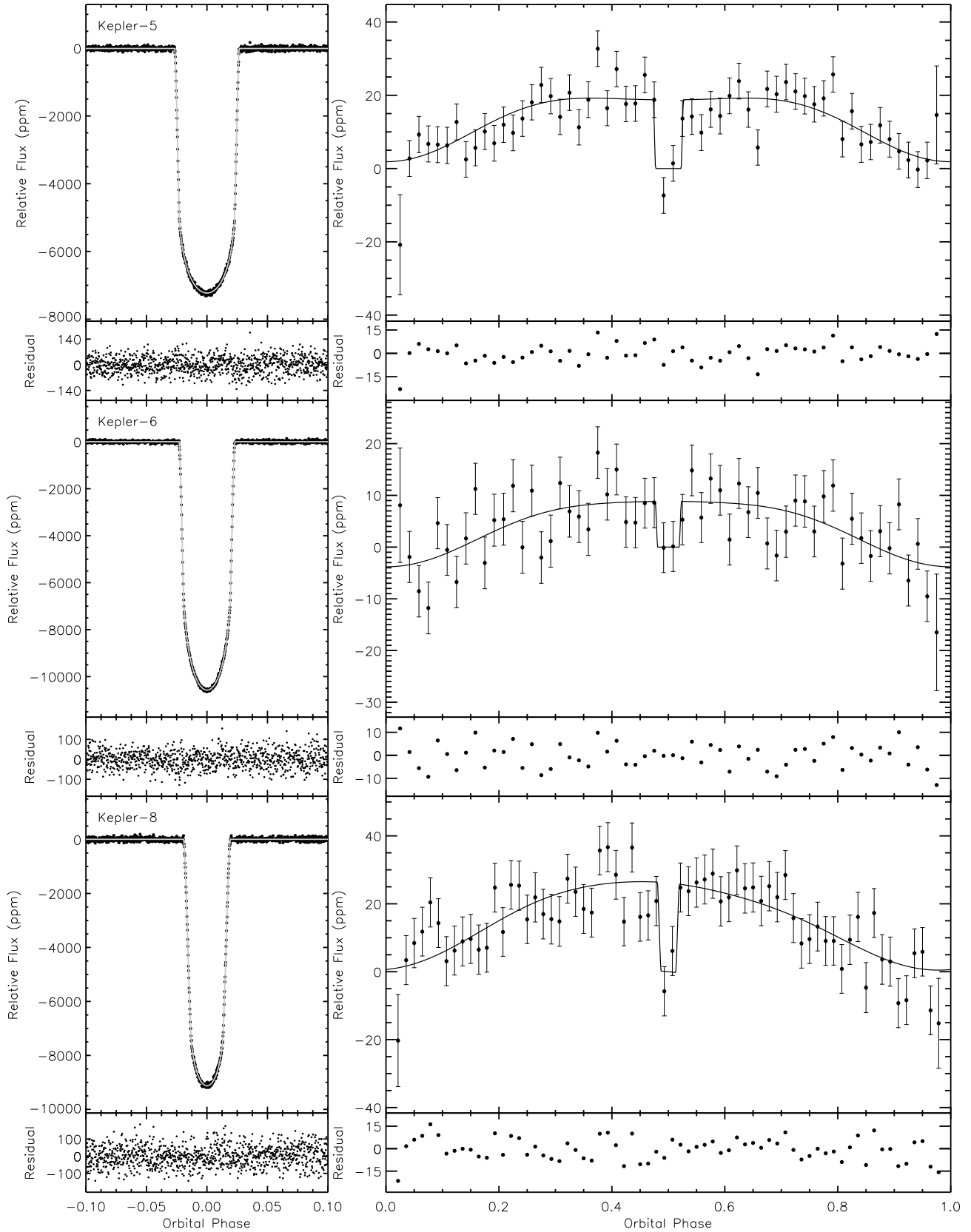


FIG. 1.— The *left* and *right* panels contain the binned and phase-folded transit light curves and phase curves, respectively. Over-plotted on each is our best fit model with the residual plotted underneath. For Kepler-5, Kepler-6 and Kepler-8 the transit bin size is 30 seconds while the phase curve bin sizes are 85, 78 and 72 minutes, respectively.

(See Sec. 4.1).

Our secondary eclipse and phase function values of Kepler-5, Kepler-8, KOI-64, TrES-2 agree with previous studies, while four of the six previous studies of HAT-P-7 are within 4σ of our values. In addition, our eclipse depth for KOI-13 is within 4σ , to three previous studies, but our phase function amplitude differs greatly, partly due to contamination from KOI-13's companion. A previous study of Kepler-6 found an eclipse depth more than double our value, however a different number of observations and systematic removal method was used (See Sec. 4.4).

For KOI-13, in addition to the phase curve components described in Sec. 3, we measure an out-of-phase third cosine harmonic with an amplitude of 6.7 ± 0.3 ppm. We believe that this signal could be a perturbation of KOI-13's ellipsoidal variations caused by its spin-orbit misalignment.

For KOI-64 and KOI-2133, we derived planet masses, from ellipsoidal variations and Doppler boosting, of less

than 6 M_J. However, we found that their day- and night-side temperatures were much higher than their equilibrium temperatures and therefore they must be self-luminous objects. We conclude that KOI-64 and KOI-2133 are false-positives created by an eclipsing binary diluted by a third stellar companion or a foreground star within the same *Kepler* pixel.

For the rest of the objects, we find albedos of less than 0.3, but conclude that for TrES-2 and KOI-13 it is likely that the atmospheric layers probed in the Kepler bandpass, are hotter than the equilibrium temperature, as inferred for CoRoT-2 (Snellen et al. 2010).

We thank Marten van Kerkwijk for insightful discussions. This work was supported by grants to R.J. from the Natural Sciences and Engineering Research Council of Canada. E.d.M. is also supported in part by an Ontario Postdoctoral Fellowship.

REFERENCES

- Adams, E. R., Ciardi, D. R., Dupree, A. K., et al. 2012, *AJ*, 144, 42
- Barclay, T., Huber, D., Rowe, J. F., et al. 2012, *ApJ*, 761, 53
- Barnes, J. W., Linscott, E., & Shporer, A. 2011, *ApJS*, 197, 10
- Batalha, N. M., Rowe, J. F., Bryson, S. T., et al. 2013, *ApJS*, 204, 24
- Bloemen, S., Marsh, T. R., Østensen, R. H., et al. 2011, *MNRAS*, 410, 1787
- Borucki, W. J., Koch, D., Jenkins, J., et al. 2009, *Science*, 325, 709
- Borucki, W. J., Koch, D. G., Basri, G., et al. 2011, *ApJ*, 736, 19
- Burrows, A., Ibgui, L., & Hubeny, I. 2008, *ApJ*, 682, 1277
- Claret, A., & Bloemen, S. 2011, *A&A*, 529, A75
- Collier Cameron, A., Horne, K., Penny, A., & Leigh, C. 2002, *MNRAS*, 330, 187
- Coughlin, J. L., & López-Morales, M. 2012, *ApJ*, 750, 100
- Cowan, N. B., & Agol, E. 2011, *ApJ*, 726, 82
- Croll, B., Albert, L., Lafreniere, D., Jayawardhana, R., & Fortney, J. J. 2010, *ApJ*, 717, 1084
- Daemgen, S., Hormuth, F., Brandner, W., et al. 2009, *A&A*, 498, 567
- de Mooij, E. J. W., & Snellen, I. A. G. 2009, *A&A*, 493, L35
- Deming, D. 2009, in *IAU Symposium*, Vol. 253, *IAU Symposium*, ed. F. Pont, D. Sasselov, & M. J. Holman, 197–207
- Désert, J.-M., Charbonneau, D., Fortney, J. J., et al. 2011, *ApJS*, 197, 11
- Dunham, E. W., Borucki, W. J., Koch, D. G., et al. 2010, *ApJ*, 713, L136
- Fanelli, M. N., Jenkins, J. M., Bryson, S. T., et al. 2011, *Kepler Data Processing Handbook*, NASA Ames Research Center
- Gelman, A., & Rubin, D. B. 1992, *Stat. Sci.*, 7, 457
- Hauschildt, P. H., Allard, F., Ferguson, J., Baron, E., & Alexander, D. R. 1999, *ApJ*, 525, 871
- Jackson, B. K., Lewis, N. K., Barnes, J. W., et al. 2012, *ApJ*, 751, 112
- Jenkins, J. M., Borucki, W. J., Koch, D. G., et al. 2010, *ApJ*, 724, 1108
- Kipping, D. M., & Spiegel, D. S. 2011, *MNRAS*, 417, L88
- Knutson, H. A., Charbonneau, D., Allen, L. E., et al. 2007, *Nature*, 447, 183
- Koch, D. G., Borucki, W. J., Rowe, J. F., et al. 2010, *ApJ*, 713, L131
- Leigh, C., Collier Cameron, A., Horne, K., Penny, A., & James, D. 2003, *MNRAS*, 344, 1271
- Loeb, A., & Gaudi, B. S. 2003, *ApJ*, 588, L117
- López-Morales, M., & Seager, S. 2007, *ApJ*, 667, L191
- Mandel, K., & Agol, E. 2002, *ApJ*, 580, L171
- Mazeh, T., Nachmani, G., Sokol, G., Faigler, S., & Zucker, S. 2012, *A&A*, 541, A56
- Mislis, D., Heller, R., Schmitt, J. H. M. M., & Hodgkin, S. 2012, *A&A*, 538, A4
- Mislis, D., & Hodgkin, S. 2012, *MNRAS*, 422, 1512
- Morris, B. M., Mandell, A. M., & Deming, D. 2013, *ApJ*, 764, L22
- Morris, S. L. 1985, *ApJ*, 295, 143
- Narita, N., Kudo, T., Bergfors, C., et al. 2010, *PASJ*, 62, 779
- O'Donovan, F. T., Charbonneau, D., Mandushev, G., et al. 2006, *ApJ*, 651, L61
- Pál, A., Bakos, G. Á., Torres, G., et al. 2008, *ApJ*, 680, 1450
- Quintana, E. V., Rowe, J. F., Barclay, T., et al. 2013, *ArXiv e-prints*
- Rowe, J. F., Matthews, J. M., Seager, S., et al. 2006, *ApJ*, 646, 1241
- Russell, H. N. 1916, *ApJ*, 43, 173
- Shporer, A., Jenkins, J. M., Rowe, J. F., et al. 2011, *AJ*, 142, 195
- Snellen, I. A. G., de Mooij, E. J. W., & Albrecht, S. 2009, *Nature*, 459, 543
- Snellen, I. A. G., de Mooij, E. J. W., & Burrows, A. 2010, *A&A*, 513, A76
- Sozzetti, A., Torres, G., Charbonneau, D., et al. 2007, *ApJ*, 664, 1190
- Still, M., & Barclay, T. 2012, *PyKE: Reduction and analysis of Kepler Simple Aperture Photometry data*, astrophysics Source Code Library
- Szabó, G. M., Szabó, R., Benkő, J. M., et al. 2011, *ApJ*, 736, L4
- Van Eylen, V., Kjeldsen, H., Christensen-Dalsgaard, J., & Aerts, C. 2012, *Astronomische Nachrichten*, 333, 1088
- Welsh, W. F., Orosz, J. A., Seager, S., et al. 2010, *ApJ*, 713, L145
- 0.8 Zechmeister, M., & Kürster, M. 2009, *A&A*, 496, 577

APPENDIX

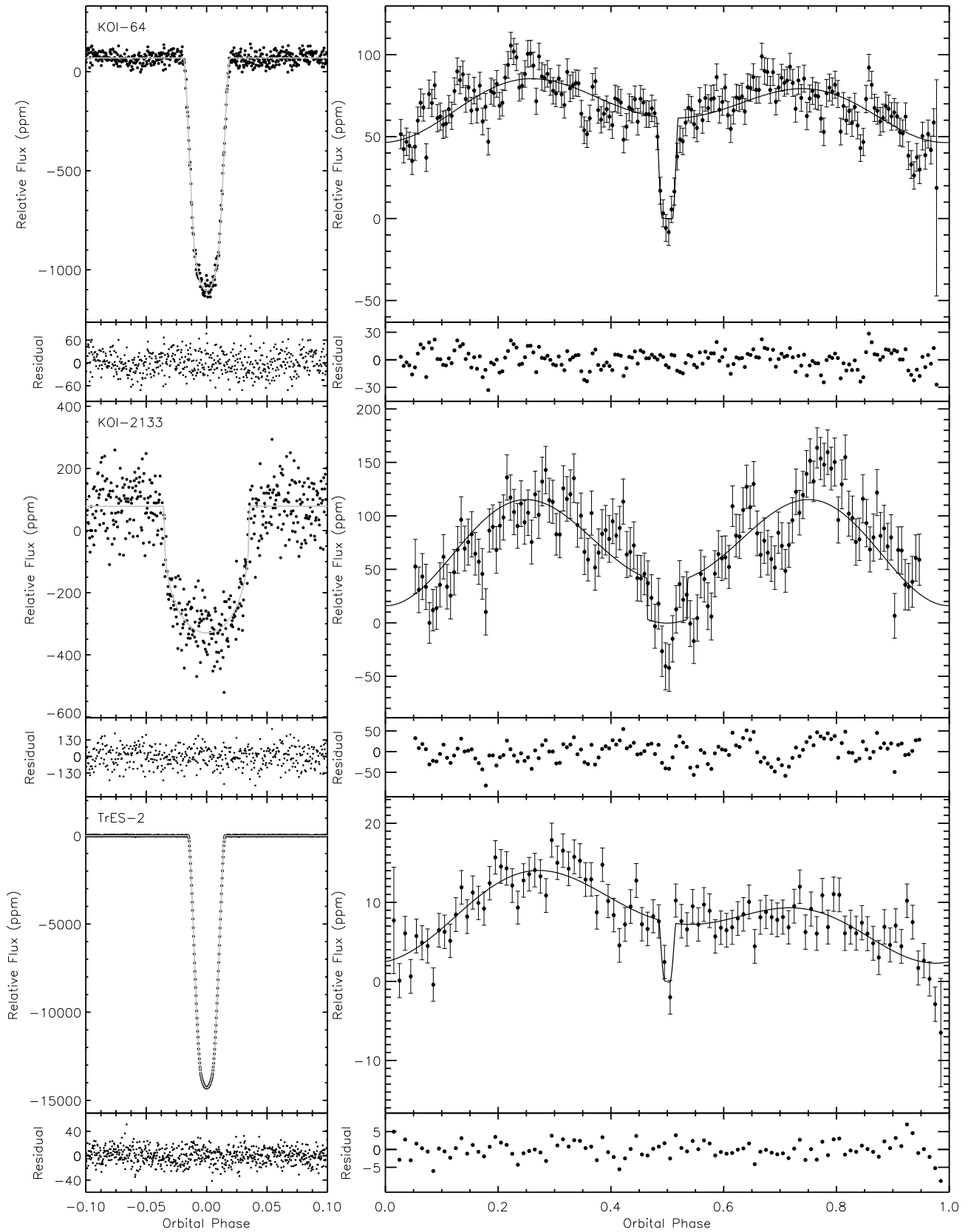


FIG. 2.— Same as 1. However, for KOI-64, KOI-2133 and TrES-2 the transit bin sizes are 30, 120 and 30 seconds, respectively, while the phase curve bin sizes are 14, 56 and 30 minutes, respectively.

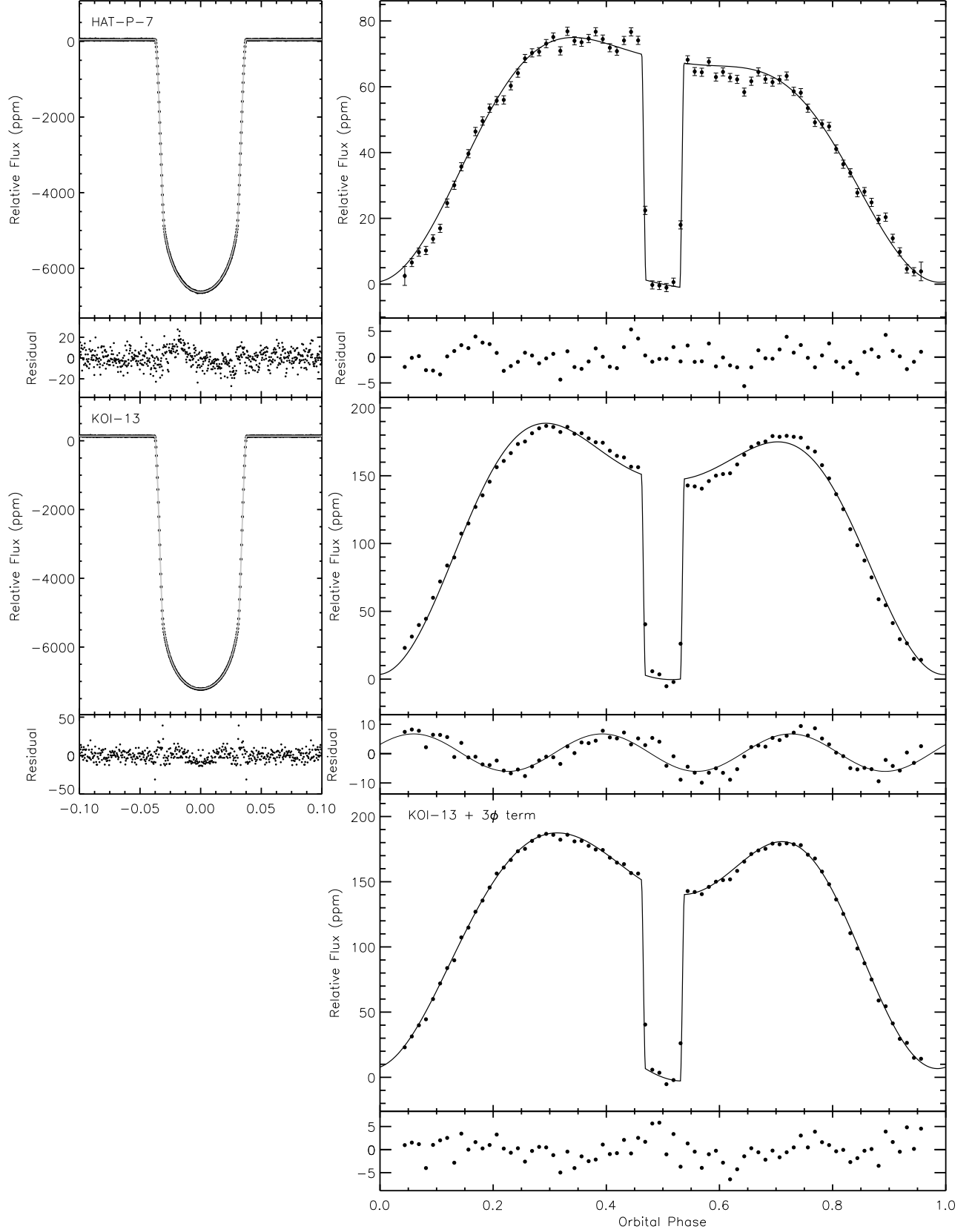


FIG. 3.— Same as 1. However, for HAT-P-7 and KOI-13 the transit bin size is 30 seconds while the phase curve bin sizes are 30 and 32 minutes, respectively. In addition, over-plotted on KOI-13's (*middle right panel*) residual is the 3ϕ signal described in Sec. 4.2. The *lower right panel* contains the best fit model and residual for a model fit including this additional signal.

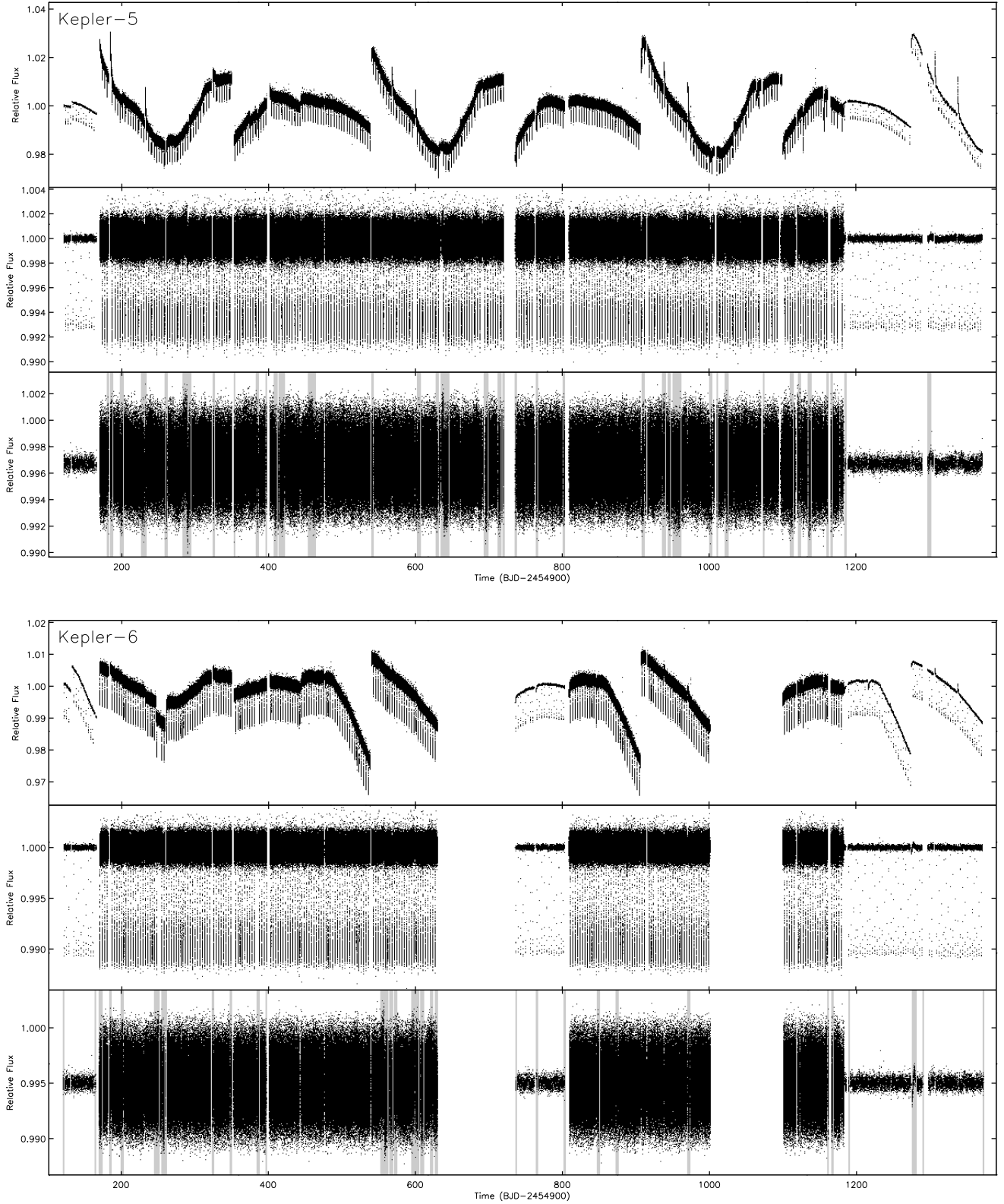


FIG. 1.— For Kepler-5 (*top* plot) and Kepler-6 (*bottom* plot), the *top* panel contains the raw SAP light curve, the *middle* panel is after cotrending and the *bottom* panel is after cotrending and removing the transits and outliers. The shaded portions indicate where we removed orbits because of a poor CBV fit.

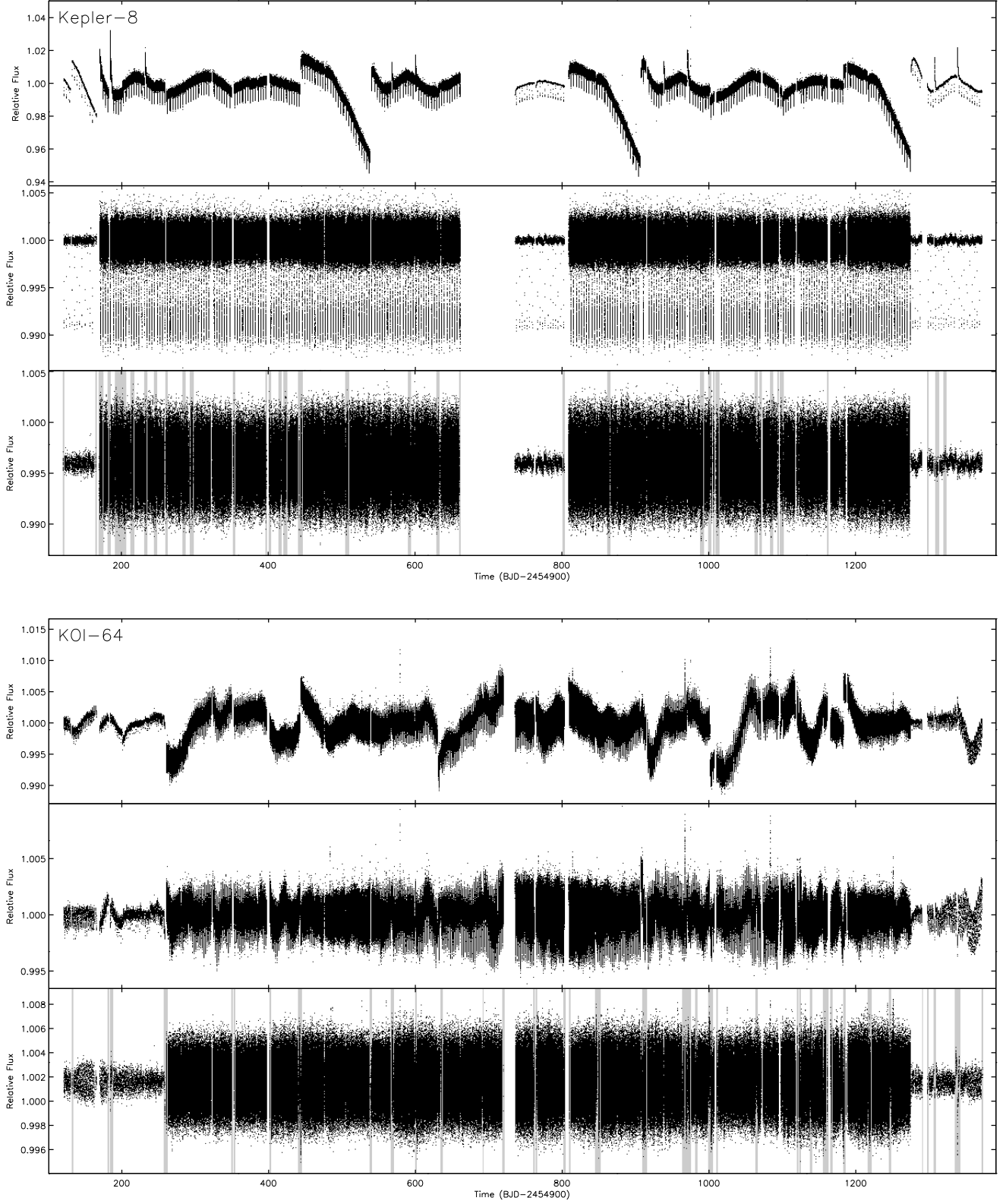


FIG. 2.— Same as Fig.1, but for Kepler-5 (*top* plot) and KOI-64 (*bottom* plot) and where, for KOI-64, the *bottom* panel contains the cotrended/out-of-transit/outlier-filtered light curve after stellar variability removal (as described in Sec. 2.3).

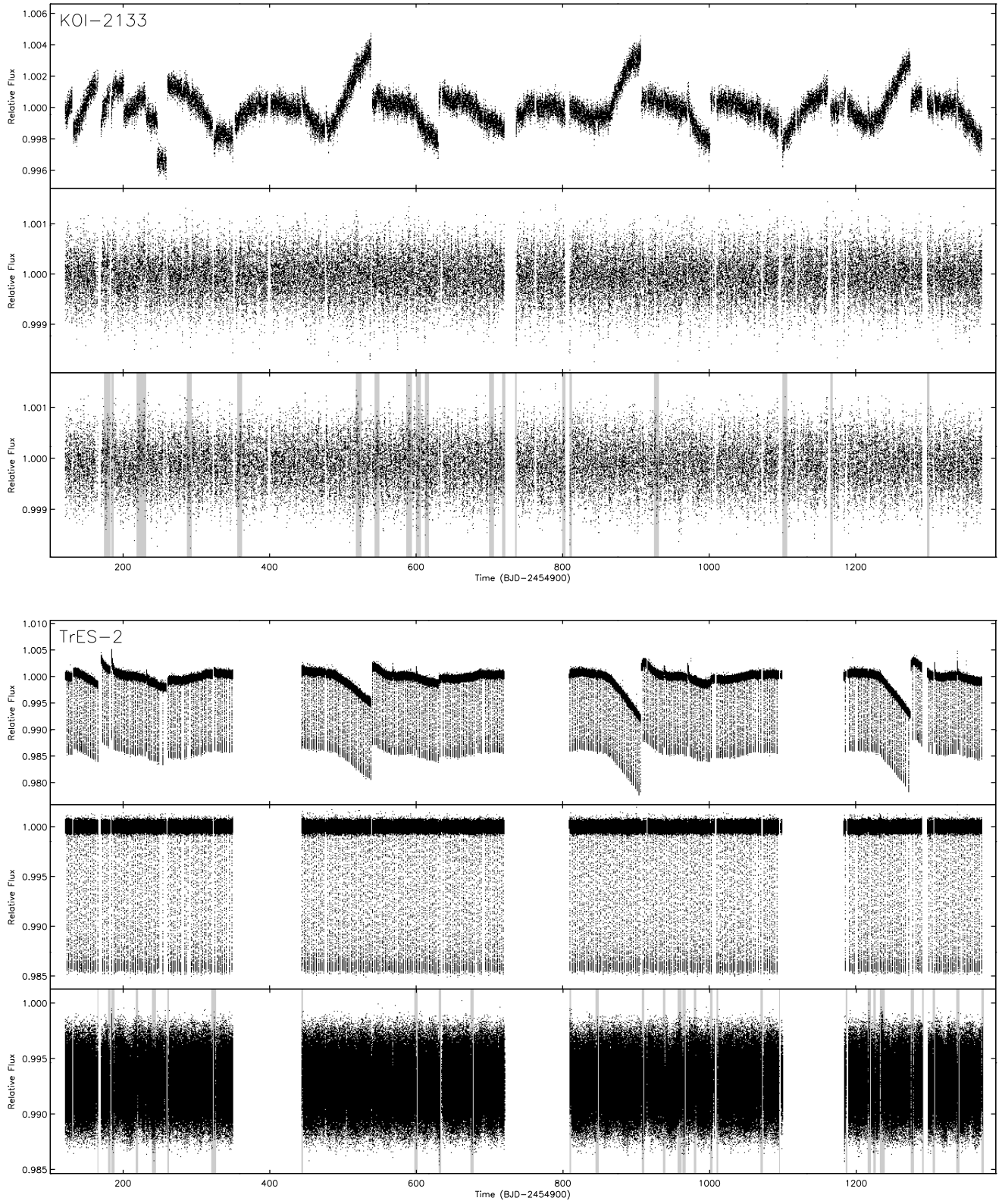


FIG. 3.— Same as Fig.1, but for KOI-2133 (*top plot*) and TrES-2 (*bottom plot*).

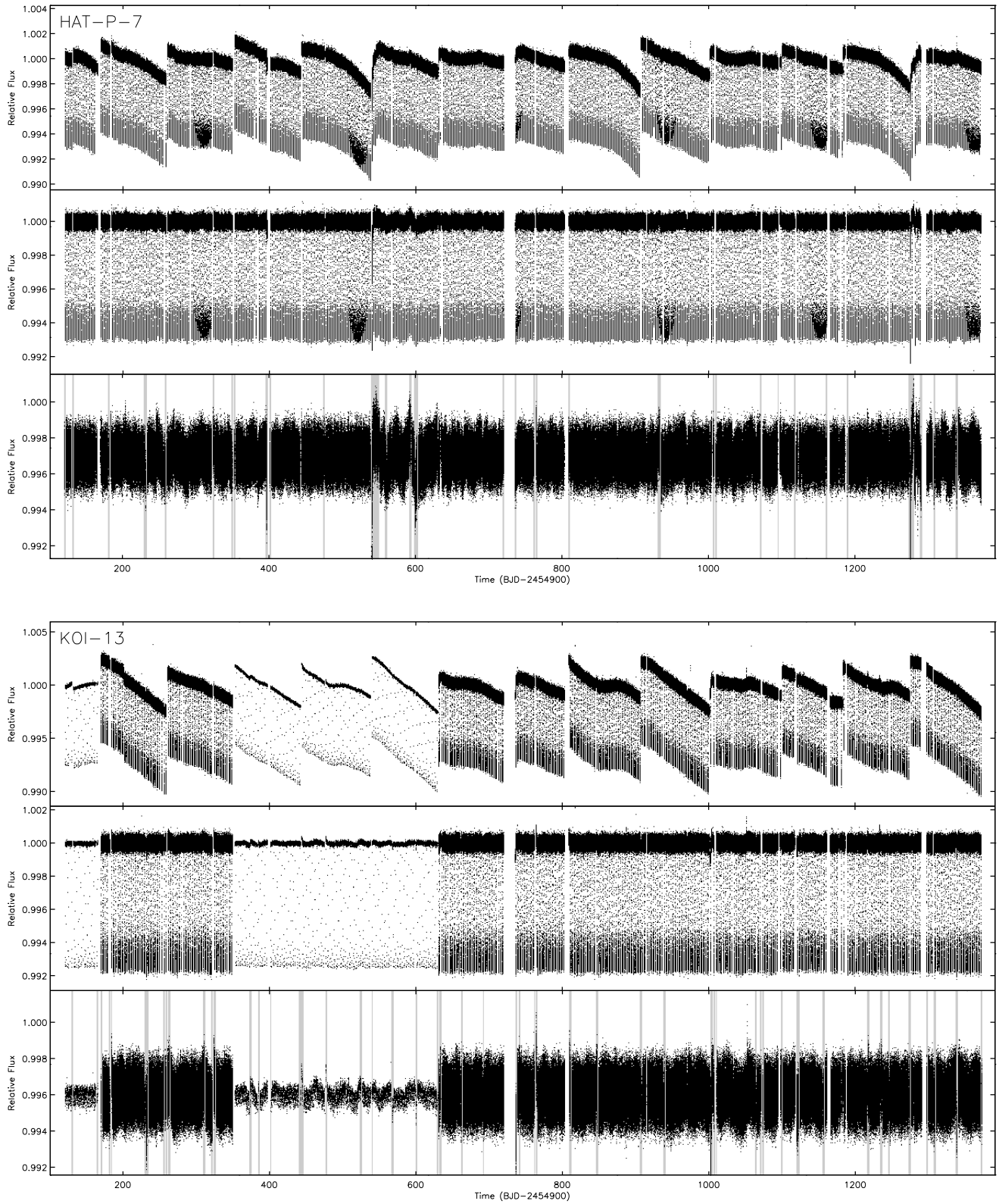


FIG. 4.— Same as Fig.1, but for HAT-P-7 (*top plot*) and KOI-13 (*bottom plot*).